Congenital disorder of glycosylation caused by starting site-specific variant in syntaxin-5

Peter T.A. Linders[1], Eveline C.F. Gerretsen[1], Angel Ashikov[2,3], Mari-Anne Vals[4,5], Natalia H. Revelo[1], Richard Arts[1], Melissa Baerenfaenger[2], Fokje Zijlstra[3], Karin Huijben[3], Kimiyo Raymond[6], Kai Muru[5,7], Olga Fjodorova[7], Sander Pajusalu[5,7], Katrin Õunap[5,7], Martin ter Beest[1], Dirk Lefeber[2,3,*] and Geert van den Bogaart[1,8,*]

[1] Department of Tumor Immunology, Radboud University Medical Center, 6525 GA Nijmegen, The Netherlands

[2] Department of Neurology, Donders Institute for Brain, Cognition and Behavior, Radboud University Medical Center, 6525 GA, Nijmegen, The Netherlands

[3] Translational Metabolic Laboratory, Department of Laboratory Medicine, Radboud University Medical Center, 6525 GA, Nijmegen, The Netherlands

[4] Children's Clinic, Tartu University Hospital, Estonia

[5] Department of Clinical Genetics, Institute of Clinical Medicine, University of Tartu, Estonia

[6] Department of Laboratory Medicine and Pathology, Mayo College of Medicine, Rochester, Minnesota, USA.

[7] Department of Clinical Genetics, United Laboratories, Tartu University Hospital, Tartu, Estonia

[8] Department of Molecular Immunology, Groningen Biomolecular Sciences and Biotechnology Institute, University of Groningen, 9747AG, Groningen, Netherlands

[*] Correspondence: dirk.lefeber@radboudumc.nl; Tel.: +31-24-36-14567; g.van.den.bogaart@rug.nl; Tel.: +31-50-36-35230

Abstract

The SNARE (soluble N-ethylmaleimide-sensitive factor attachment protein receptor) protein syntaxin-5 (Stx5) is essential for Golgi transport. In humans, the *STX5* mRNA encodes two protein isoforms, Stx5 Long (Stx5L) from the first starting methionine and Stx5 Short (Stx5S) from an alternative starting methionine at position 55. In this study, we identified a novel human disorder caused by a single missense substitution in the second starting methionine (p.M55V), resulting in complete loss of the short isoform. Patients suffer from an early fatal multisystem disease, including severe liver disease, skeletal abnormalities and abnormal glycosylation. Whereas Golgi morphology was unaltered, primary human dermal fibroblasts isolated from these patients showed defective glycosylation and mislocalization of glycosyltransferases. Measurements of anterograde

trafficking, based on biotin-synchronizable forms of Stx5 (the RUSH system), and of cognate binding SNAREs, based on Förster resonance energy transfer (FRET), revealed that the short isoform of Stx5 is essential for intra-Golgi transport. This is the first time a mutation in an alternative starting codon is linked to human disease, demonstrating that the site of translation initiation is an important new layer of regulating protein trafficking.

Keywords

Syntaxin-5, ER-Golgi trafficking, glycosylation, secretory pathway, congenital disorders of glycosylation

Introduction

In eukaryotes, proteins destined for the secretory pathway are synthesized at the endoplasmic reticulum (ER) and then transported to the Golgi apparatus, where they are sorted for their ultimate destinations at the *trans*-Golgi network. Central to this process is intracellular membrane fusion, which is mediated by members of the SNARE (soluble *N*-ethylmaleimide-sensitive factor attachment protein receptor) protein family. Membrane fusion is the result of the formation of a tight alpha-helical coiled-coil bundle by cognate SNARE proteins that are present in both the carrier vesicle and target membranes. Membrane fusion requires an R-SNARE, characterized by an arginine residue located central in the SNARE bundle, and three Q-SNAREs, with glutamine residues instead. For anterograde ER to Golgi trafficking, the target (t-) SNARE complex is formed by the Qa-SNARE syntaxin-5 (Stx5)[1–4], together with the Qb-SNAREs GosR1 (also known as GS27 or membrin) or GosR2 (GS28), and R-SNAREs Ykt6 or Sec22b (Ers24)[5–7]. Generally in mammalian cells, the R-SNAREs act as vesicle (v-) SNAREs and the Q-SNAREs together form the t-SNARE complex on the target membrane[8]. In contrast, the Qc-SNAREs Bet1 and Bet1L (GS15) function as the v-SNAREs at the ER/Golgi interface[9–12]. This possibly prevents the formation of non-functional SNARE complexes during ER to Golgi transit. In addition, Stx5 functions in retrograde intra-Golgi transport by forming a SNARE complex with GosR1, Bet1L, and Ykt6[12,13] and in retrograde trafficking from endosomes to the *trans*-Golgi network (TGN)[14,15], making it a unique SNARE protein involved in both anterograde and retrograde Golgi transport.

STX5 is highly conserved and is an essential gene in animals and fungi[16,17]. In animals, Stx5 exists as a long and a short isoform translated from the same mRNA: 39.6 kDa sized Stx5 Long (Stx5L) and 34.1 kDa sized Stx5 Short (Stx5S)[13,18]. This is in contrast to lower organisms such as *Saccharomyces cerevisiae*, which only expresses a single isoform of Stx5 (Sed5p), likely resembling mammalian Stx5L with the presence of an N-terminal COPI-binding tribasic motif[19]. The emergence of a second Stx5 isoform can be traced back to the pacific purple sea urchin, *Strongylocentrotus purpuratus,* and is also present in the model organism *Danio rerio*, but not in *Drosophila melanogaster* or *Caenorhabditis elegans*. Compared to Stx5S, Stx5L contains 54 extra N-terminal residues bearing an Arginine – Lysine – Arginine (RKR) ER retrieval motif, and as a result, Stx5L locates more to the ER whereas Stx5S locates more to the Golgi network[13,18,20–22]. The evolutionary necessity of Stx5L remains unclear but it has been suggested that Stx5L is important to maintain ER structure by binding microtubules, possibly via CLIMP-63[21,23]. In addition, immunoprecipitations showed that GosR1 and Bet1L preferentially interact with Stx5S over Stx5L[24,25], suggesting that Stx5S might act in more fusogenic complexes

later at the ER-Golgi interface whereas Stx5L might be more involved in earlier fusion steps. In the present study, we identified a genetic variant in the second translation codon methionine-55, fully abrogating the production of Stx5S and providing a unique opportunity to study the physiological relevance of the existence of two isoforms in humans. Patients homozygous for this mutation have a very severe clinical phenotype associated with infantile mortality and defective protein glycosylation. We demonstrate that although Stx5L can largely compensate for the lack of Stx5S, the loss of Stx5S leads to defects in anterograde Golgi trafficking with mislocalization of glycosyltransferases, which results in pronounced defects in glycosylation. Moreover, by synchronizing the intracellular trafficking of Stx5 isoforms, we reveal differential trafficking routes for either isoform and identify Stx5S as the dominant Qa-SNARE for intra-Golgi transport. This is the first time that a mutation in an alternate starting site of ribosomal translation is related to human disease. This finding reveals that protein function can be regulated at the level of translation initiation and has profound effects on intracellular membrane trafficking and Golgi function.

Results

Clinical data

The family history (Supplementary Figure 1) revealed multiple deceased individuals (IV:3, IV:9, IV:10) shortly after birth, spontaneous abortions (IV:5, IV:6, IV:7), and elective abortions in the 20th-21st week of pregnancy due to abnormal fetal ultrasound (US) (IV:4, IV:8). Fetal US of individuals IV:8, IV:9, and IV:10 (Figure 1a-c, respectively) showed shortening of the long bones with suspicion of chondrodysplasia. Patients IV:9 and IV:10 showed highly dysmorphic facial features (high forehead, frontal bossing, prominent glabella, short and upturned nose, long philtrum, micrognathia and dysplastic ears), skeletal dysplasia (short extremities and narrow thorax), profound hypotonia, hepatomegaly, and many abnormal laboratory parameters including elevated cholesterol (Figure 1b, c, Supplementary Table 1). After birth, the main clinical problem for both patients IV:9 and IV:10 was progressive liver failure with cholestasis and hyperinsulinemic hypoglycemia (Supplementary Table 1). Liver failure was the main cause of death at the age of 28 days and 8 months, in patients IV:9 and IV:10, respectively. Autopsy of fetus IV:8 revealed bilateral hydronephrosis and sacral lordosis. Autopsy of patient IV:9 showed hepatomegaly with stage 3 to 4 liver fibrosis, agenesis of left kidney, hyperemia of internal organs, ventricular septal defect and suggestive pathohistological features of

chondrodysplasia. Autopsy of patient IV:10 showed biliary cirrhosis and nodular regenerative hyperplasia, pancreatic hypertrophia/hyperplasia, and narrow thorax with normal lung development.

Abnormal protein glycosylation suggests a defect in Golgi trafficking

Known genetic causes for skeletal dysplasias were excluded (IV:8), no submicroscopic chromosomal abnormalities were found, while most metabolic investigations were normal except for the Congenital Disorders of Glycosylation (CDG) (IV:9 and IV:10). CDG screening revealed a strong hyposialylation of protein N-glycosylation and mucin-type O-glycosylation, as analyzed by isofocusing of respectively plasma transferrin (Fig 1d) and apolipoprotein CIII (ApoCIII-IEF, Fig 1e). ApoCIII-IEF showed a strong increase of non-sialylated apoCIII (ApoCIII-0), even stronger than observed for genetic defects in the Conserved Oligomeric Golgi (COG) complex, a known group of disorders with disturbed Golgi homeostasis and abnormal glycosylation. To gain more insight into the abnormal N-glycan structures, mass spectrometry was performed of intact transferrin (Fig 1f, g, Supplementary Figure 2) and of total plasma protein derived N-glycans (Fig 1f, h, Supplementary Figure 3). Analysis of intact transferrin of individuals IV:9 and IV:10 revealed multiple abnormal glycan structures, divided into two categories: high mannose structures and truncated glycans. A dominant accumulation was found of high-mannose glycans (Supplementary Table 2, Man5, mass/peak number) suggesting a problem with MGAT1, the enzyme that adds the next *N*-acetylglucosamine during N-glycosylation. Furthermore, a series of transferrin isoforms was observed with reduced incorporation of galactose and sialic acid residues. Analysis of N-glycans released from total plasma proteins recapitulated the two categories of abnormal glycans with the accumulation of high mannose glycans, as well as reduced incorporation of galactose and sialic acid residues (Supplementary Table 3).
Together, these data indicate that the activities of multiple glycosyltransferases in the Golgi apparatus are affected, covering both N- and O-glycosylation, thereby suggesting a general disturbance in Golgi trafficking.

Molecular investigations result in the identification of variants in STX5

Chromosomal microarray analysis (CMA) using HumanCytoSNP-12 microarrays revealed multiple long contiguous stretches of homozygosity (LCSH, >5 Mb) distributed across the entire genome, with several regions of homozygosity on chromosome 11 in all three affected sibs (IV:8, IV:9 and IV:10, Supplementary Table 4). Exome sequencing was performed in proband IV:9 to find the genetic variant that could be associated

with the disease. Only two homozygous rare protein-altering variants without homozygous individuals in the gnomAD v3 database were identified in shared homozygous stretches on chromosome 11. First, a missense variant in the *VPS37C* gene was discovered (NM_017966.4:c.760G>T p.(Gly254Cys) rs201088253). However, as this variant reaches an allele frequency of 0.9% in Estonia, it is unlikely to cause a rare genetic disorder. The second variant was identified in the *STX5* gene (NM_003164.4:c.163A>G p.(Met55Val), Fig 2a). This is a missense mutation affecting the alternative starting codon for the production of the short Stx5 isoform. The variant is absent from the gnomAD v3 database and was thus classified as a potentially disease-causing variant. The variant was confirmed by Sanger sequencing as homozygous in all affected individuals (IV:8, IV:9, and IV:10) and as heterozygous in the mother (III:2). Paternal DNA was not available for testing.

To confirm the effect of the genetic variant on both Stx5 proteoforms, immunoblotting was performed in primary dermal fibroblasts of patients IV:9 and IV:10. While Stx5L was present, a total absence of Stx5S was found in both patient fibroblasts (Fig. 2b, c). We next tested the expression of known interaction partners of Stx5. The levels of Qc-SNARE Bet1L (Fig. 2b, c), which forms a complex with Stx5 upon retrograde intra-Golgi trafficking[12–15], were also reduced. In contrast, the expression of Qc-SNARE Bet1, which forms a complex with Stx5 upon anterograde ER-Golgi trafficking[5,7,13,26] was not reduced (Fig. 2b, c). Likewise, the expression of Qb-SNAREs GosR1 and GosR2, which can complex with Stx5 for anterograde ER-Golgi trafficking and retrograde intra-Golgi trafficking[4,5,7,12,13,24] were unaltered in patient dermal fibroblast lysates. We hypothesized that a compensatory mechanism might exist by upregulating the expression of the *trans*-Golgi Qa-SNARE Stx16[27], usually involved in endosome-to-TGN trafficking[28], but we did not detect a change of Stx16 expression in patient fibroblast lysates (Fig. 2b, c). As a first step to confirm that fibroblasts offer a useful model to recapitulate the cell biological abnormalities due to loss of the Stx5S isoform, we studied glycosylation by fluorescently-labeled lectins.

Glycosylation defects in Stx5M55V patient fibroblasts

Cell surface staining with the lectin SNA-I from *Sambucus nigra*, which binds terminal sialic acid in an α-2,6 linkage of fully-formed N-glycan moieties and, to a lesser extent, sialic acid in an α-2,3 linkage, showed that glycosylation was also impaired at the cellular level in patient fibroblasts. Compared to fibroblasts of healthy donors, we observed a more than two-fold reduced SNA-I labeling intensity in Stx5M55V patient fibroblasts (Fig. 2d,e). To confirm this glycosylation defect, we performed cell surface staining with the lectin PNA (Peanut

agglutinin) from *Arachis hypogaea*, which binds terminal galactose residues present on mucin O-glycan moieties. Opposite to our findings with SNA-I, we observed an increased labeling intensity in Stx5M55V patient fibroblasts relative to healthy control by about eight-fold (Fig. 2f,g). As these results reiterate the glycosylation defect observed on serum transferrin, total plasma N-glycans and apoCIII mucin O-glycans, using patient fibroblasts is a suitable model to investigate the cell biological consequences of the complete disruption of the Stx5S isoform.

Stx5M55V mutation results in mislocalization of glycosyltransferases

Given that Stx5 mediates ER-Golgi trafficking[2,4–7,12,13,15,24,26], we next investigated whether the glycosylation defect in Stx5M55V patient fibroblasts was caused by the mislocalization of glycosyltransferases. We performed immunofluorescence labeling of mannosyl (α-1,3-)-glycoprotein β-1,2-*N*-acetylglucosaminyltransferase (MGAT1, also known as GnTI), which catalyzes the addition of GlcNAc to the immature man-5 N-glycan. Compared to healthy donor fibroblasts, MGAT1 colocalizes only slightly less with the *cis*-Golgi marker GM130 in patient fibroblasts (Supplementary Fig. 4a, b), but colocalized substantially less with the *trans*-Golgi network marker TGN46 (Fig. 3a, b). In contrast, alpha-mannosidase 2 (MAN2A1), which catalyzes the final hydrolytic step in the N-glycan maturation pathway after MGAT1 conversion, colocalized substantially less with both GM130 (Fig. 3c, d) and TGN46 (Supplementary Fig. 4c, d). Similarly to MGAT1, beta-galactoside alpha-2,6-sialyltransferase 1 (ST6GAL1), which catalyzes the transfer of sialic acid to galactose residues of N-glycans in an α-2,6 linkage, colocalized less with both GM130 (Supplementary Fig. 4e, f) and TGN46 (Supplementary Fig. 4g, h). Finally, *N*-acetylgalactosaminyltransferase 2 (GALNT2), which catalyzes the initial reaction in mucin O-linked glycan synthesis, localized more to the *cis*-Golgi (marker Zinc finger protein-like 1 (ZFPL1)[29]) (Fig. 3e, f) and less to the *trans*-Golgi (Fig. 3g, h).

Taken together, the loss of Stx5S results in irregular localization of glycosyltransferases to the Golgi apparatus. Mislocalization of glycosyltransferases can have a profound impact on glycosylation as shown by computational simulations[30]. Notwithstanding these large defects in glycosylation in the Stx5M55V patients, negative staining electron microscopy and immunofluorescence labeling of *cis*- and *trans*-Golgi markers showed no large alterations in Golgi morphology and the polarized arrangement of Golgi apparatus cisternae was still present in Stx5M55V fibroblasts (Supplementary Figure 5). These results indicate that although Stx5L

is sufficient to maintain normal Golgi apparatus morphology, Stx5S is required for proper trafficking of glycosylation enzymes.

Stx5 mediates retrograde Golgi trafficking

As Stx5 is required for trafficking of glycosylation enzymes, we then studied the role of the two Stx5 isoforms in ER-Golgi trafficking. Because Stx5L contains an RKR ER-retrieval motif in its N-terminal extension, it locates more at the ER compared to Stx5S[13,18,20,21]. In line with this, we observed a more dominant localization of Stx5L at the ER and less at various Golgi compartments in Stx5M55V fibroblasts compared to total Stx5 localization in healthy control fibroblasts (Fig. 4a, b, d, e, Supplementary Fig. 6a, b, d, e). A notable difference was the far more diffuse staining in Stx5M55V patients of the COPI coat protein βCOP (Fig. 4a, c) and of TGN46 (Fig. 4d, f). In contrast, we observed a small increase in GM130 fluorescence in Stx5M55V patients (Supplementary Fig. 6f). Western blot showed that total cellular levels of βCOP and GM130 were not altered in Stx5M55V patients (Fig. 4g). In contrast, total TGN46 protein levels were reduced in patient fibroblasts (Fig. 4h). These findings suggest that loss of Stx5S results in reduced COPI trafficking between GM130-marked *cis*- and TGN46-marked *trans*-Golgi compartments. As COPI is also involved in retrograde Golgi-ER transport[31], we investigated whether trafficking at this interface is compromised in Stx5M55V fibroblasts by using the fungal metabolite Brefeldin A (BFA), which inhibits COPI vesicle formation[32]. If loss of Stx5S results in reduced retrograde Golgi-ER transport, we expect reduced relocalization of Golgi-resident proteins to ER upon BFA treatment. Indeed, redistribution of GALNT2 from the Golgi to the ER was incomplete in patient fibroblasts (Fig. 5a, b), showing a role for Stx5S in retrograde COPI trafficking. To delineate the role of Stx5L in this process, we generated two clonal HeLa cell lines lacking Stx5L by CRISPR/Cas9 (Stx5ΔL: B1A7 and C1F4). In these cells, BFA resulted in faster relocalization of GALNT2 to the ER compared to parental HeLa (Fig. 5c, d), indicating that Stx5S suffices for retrograde COPI trafficking and the expression of Stx5L is rate-limiting for this process. Further investigation of anterograde trafficking in Stx5ΔL cells with H-89 washout (Supplementary fig. 7a, b), the RUSH system for synchronized ER-Golgi transport[33] (Supplementary fig. 7c, d, Supplementary movies 1, 2) and temperature-synchronizable VSVG[34] (Supplementary fig. 7e, f, Supplementary movies 3, 4) revealed no phenotype relating to the loss of Stx5L. Thus, these data suggest Stx5L has no necessary function in ER-Golgi trafficking as Stx5S can compensate, while Stx5L can only partly compensate for the loss of Stx5S.

Discerning the roles of Stx5 isoforms in ER and Golgi trafficking

Our results in patient fibroblasts indicate a differential trafficking role of the two Stx5 isoforms in anterograde ER to Golgi trafficking. To gain more insight in this process, we fused each Stx5 isoform to streptavidin-binding protein (SBP) and mCitrine (Stx5L-SBP-mCitrine and Stx5S-SBP-mCitrine). Moreover, we generated a mutant form of Stx5L where the RKR ER-retrieval motif was converted to 3x alanine (AAA) (Stx5LΔER-SBP-mCitrine)[18], to delineate the role of this motif in ER-Golgi transport. The co-expression of these constructs with ER-localized streptavidin enabled the synchronized release of the Stx5 fusion proteins from the ER using biotin, which is the so-called RUSH system[33] (Fig. 6a). Co-expressing each Stx5 isoform with the Golgi marker Giantin fused to mScarlet[35] in wildtype HeLa cells, allowed to visualize the trafficking of Stx5-SBP-mCitrine to the Golgi following the addition of biotin (Fig. 6a, b, Supplementary movies 5-7). All three Stx5 isoforms reached the Golgi with the same rate and achieved maximal Golgi localization after 20 minutes (Fig. 6c). However, the subsequent decrease in Golgi localization, attributed to recycling to the ER or probable degradation of the fusion proteins, was faster for Stx5L-SBP-mCitrine than for than for Stx5S or Stx5LΔER (Fig. 6c). Thus, the RKR ER retrieval motif of Stx5L is necessary and sufficient for the attenuated presence of Stx5L at the Golgi, supporting that the main role of Stx5S is COPI trafficking specifically at the Golgi.

The two isoforms of Stx5 differently engage in SNARE complexes

Since interactions of Stx5 with Bet1 and Bet1L mediate anterograde ER-Golgi transport and retrograde intra-Golgi transport, respectively[9–12], we hypothesized that Stx5S would interact more strongly with Bet1L, whereas Stx5L would interact more strongly with Bet1. We set out to test this hypothesis by performing co-immunoprecipitation with our RUSH Stx5 constructs. However, we were unable to resolve differences in binding to endogenous cognate Qc-SNAREs between the two Stx5 isoforms, either without or with 30 mins biotin (Supplementary Fig. 8a, b). A likely explanation is that interactions might occur *in vitro* during the immunoprecipitation. Therefore, we developed an approach to visualize SNARE complexes based on a combination of the RUSH system[33] and our previously developed Förster resonance energy transfer-fluorescence lifetime imaging microscopy (FRET-FLIM) approach for visualization of SNARE complexes[36] (Fig. 7a). The FRET-FLIM approach employed Stx5 isoforms C-terminally fused with a donor fluorophore (mCitrine) and Bet1L C-terminally fused with an acceptor fluorophore (mCherry). The formation of a post-fusion SNARE complex results in the close proximity of the donor and an acceptor fluorophore resulting in FRET which can be measured from a decreased donor fluorescence lifetime (τ). Contrary to ratiometric FRET, FRET-FLIM is not

dependent on local concentration differences or excitation intensities of the donor and acceptor fluorophores, as τ is an intrinsic property of the fluorophore itself. By combining the FRET-FLIM approach with the RUSH system, we were able to control the spatial localization of Stx5 isoforms and measure interactions specifically at the ER (no biotin) or the Golgi apparatus (20 min after biotin addition). 30 minutes prior to imaging, cells were incubated with cycloheximide in culture medium to make sure background interaction from any ER-localized newly synthesized acceptor construct was mitigated.

For the mCitrine donor-only Stx5 constructs, we measured similar lifetimes for both isoforms (Fig. 7c, Supplementary Fig. 9a, Stx5L: 3.02 ns ± 0.004, Stx5S: 2.99 ns ± 0.007) prior to biotin addition, while these lifetimes slightly decreased following biotin addition (Fig. 9d, Supplementary Fig. 9a, Stx5L: 2.90 ns ± 0.006, Stx5S: 2.86 ns ±0.011). We attribute this reduced lifetime to the fact that mCitrine is somewhat pH-sensitive[37] and the pH of the Golgi apparatus is lower than in the ER lumen[38]. We then co-expressed the Stx5 isoforms with mCherry-tagged Bet1L (Bet1L-mCherry) (Fig. 7a,b). At the ER, thus before the release of Stx5 with biotin, we observed reduced lifetimes for both Stx5S and Stx5L with Bet1L-mCherry, compared to the donor-only controls (Fig. 7b, c, Supplementary fig. 9b, Stx5L: 2.82 ns ± 0.01, Stx5S: 2.79 ± 0.01), whereas the lifetimes of Stx5S and Stx5L did not significantly differ from each other. After the release in the presence of biotin, this difference between Stx5L and Stx5S became significant and lifetimes were 2.63 ns (± 0.01) for Stx5L while Stx5S dropped to 2.52 ns (± 0.03) (Fig. 7b, d, Supplementary fig. 9c). To validate that the observed effect is indeed caused by functional SNARE complex formation, we repeated this experiment with VAMP8 instead of Bet1L as the acceptor R-SNARE. VAMP8 has no role in ER-Golgi membrane fusion but rather associates with the late endosomal/lysosomal compartment[28,36,39–43]. We only observed minor decreases in fluorescence lifetimes for both Stx5L and Stx5S (Supplementary fig. 9d, e, g, prior to biotin Stx5L: 2.92 ns ± 0.01, Stx5S: 2.86 ± 0.02, upon biotin addition Supplementary fig. 9d, f, h, Stx5L: 2.82 ns ± 0.01, Stx5S: 2.76 ± 0.02). The FLIM results with VAMP8 demonstrate that Stx5S interacts more strongly with Bet1L at the Golgi than Stx5L. Thus, Stx5S is the dominant Qa-SNARE for intra-Golgi trafficking.

Discussion

Since the advent of the genomic age, close to 6000 monogenic disorders have been discovered[44]. While nearly all of these disorders result in a truncated, unstable and/or nonfunctional protein, e.g. due to a genetic variant in the catalytic site or protein misfolding, isoform-specific mutations are rare. Here we present the first known

mutation in an alternate site of ribosomal translation leading to human disease, namely the mutation of the second starting methionine of Stx5. This mutation leads to the complete and specific loss of Stx5S. Although *STX5* is an essential gene for embryonic development in mice[16,17], here we show that in humans the loss of Stx5S still allowed a completed pregnancy. Nevertheless, patients have a very severe clinical pathology characterized by infantile mortality due to liver disease, skeletal abnormalities and protein glycosylation defects. While the exact mechanism for alternative translation is unclear, this might be an actively regulated process. It could also be simply regulated by the affinity of the ribosome for the nucleotide sequence upstream of the starting codon. Supporting the latter option, analysis of translation initiation sites with NetStart[45] revealed that the starting codon of Stx5S is located in a more optimal nucleotide context than the starting codon for Stx5L (Supplementary fig. 10). This could lead to more leaky ribosomal scanning[46,47], resulting in a lower expression of Stx5L than Stx5S in controls.

Cofractionation and microscopy studies have revealed that the localization of Stx5L and Stx5S overlap to a large extent, but that they are generally distributed as a gradient between ER, ERGIC, and Golgi apparatus[20]. This observation has previously led to the suggestion that Stx5L might play a role in early Golgi trafficking, while Stx5S functions in late Golgi trafficking[2,4–7,12,13,15,24,26]. Our data now shows that this is not the case and that both Stx5 isoforms can mediate both early and late anterograde and retrograde trafficking with sufficient fidelity to keep the layered Golgi morphology intact. However, the role of Stx5S is more important for anterograde trafficking, and its absence leads to an altered Golgi distribution of glycosylation enzymes and trafficking proteins. In contrast, loss of Stx5L leads to faster anterograde trafficking suggesting it might be more involved in retrograde trafficking and/or sequestering interactions partners of Stx5S. The dominant role of Stx5S in intra-Golgi trafficking is corroborated by the observation that cellular levels of Bet1L, with known roles in intra-Golgi trafficking, are lower in Stx5M55V patient cells. Interestingly, genetic variants in conserved oligomeric Golgi (COG) tethering complex components, which are also implicated in CDGs, resulted in lower levels of Bet1L as well[48]. Although the Stx5-Bet1L interaction has been reported in several studies[14,31], our study now shows this interaction *in situ* using FLIM. This interaction is localization dependent and occurs mostly when Stx5 is localized at the Golgi. Moreover, we observed stronger interaction of Bet1L with Stx5S compared to Stx5L at the Golgi, which is likely the result of the differential localization of both isoforms.

An important function of the Golgi apparatus is protein glycosylation[49]. Collectively, somatic mutations affecting glycosylation are classified as CDGs and currently over 100 monogenic diseases affecting

297 glycosylation have been identified[50,51]. A significant number of these include defects in Golgi trafficking, such
298 as the components of the conserved oligomeric Golgi tethering complex (COG)[52–60], mutations in genes coding
299 for the vacuolar H^+-ATPase and its assembly factors[61–64], and novel genes involved in Golgi ion homeostasis[65–
300 67]. Furthermore, defects are known in components associated with COPI-coated vesicles[68] that result in
301 deficient protein glycosylation in patient cells, but are not linked to abnormal glycosylation of proteins in
302 plasma and thus escape routine CDG screening. Our study is the first example of an ER-Golgi SNARE being
303 implicated in CDG, thus highlighting the potential of glycosylation screening in patients to uncover novel cell
304 biological mechanisms.
305 While the cellular effects of the loss of Stx5S in Stx5M55V mutant fibroblasts are subtle, there can be
306 pronounced consequences in secretory cells, such as exocrine and endocrine cells, which are sensitive to
307 minor disruptions of the secretory pathway[49,68–70]. Recent modeling showed that the slight mislocalization of
308 glycosyltransferases can result in large differences in glycosylation patterns, because glycosylation is the result
309 of the sequential addition and removal of different sugar moieties at the various Golgi compartments[30]. The
310 defects in intra-Golgi trafficking can explain the other pathologies as well. For instance, Stx5 can participate in
311 the trafficking and processing of the very low-density lipoprotein receptor (VLDL-R) and this role is heavily
312 dependent on the expression of Stx5[71], thus providing an explanation for the observed cholesterol
313 homeostasis defect with elevated cholesterol in all Stx5M55V patients.
314 In summary, we have demonstrated the first known mutation in an alternative starting codon leading to
315 human disease, with severe impact on intracellular membrane trafficking and leading to the discovery of a
316 novel CDG.
317
318 **Acknowledgments**
319 We thank the family for participating in this study. We thank following people for constructs: Hesso Farhan
320 and Franck Perez (Str-KDEL_ManII-SBP-EGFP; Addgene plasmid #65252), Jennifer Lippincott-Schwartz (pEGFP-
321 VSVG; Addgene plasmid #11912) and Feng Zhang (pSpCas9n(BB)-2A-Puro (PX462) V2.0; Addgene plasmid
322 #62987). We also thank the Microscopic Imaging Center of the Radboud Institute for Molecular Life Sciences
323 for use of their microscopy facilities. N.H.R. is funded by a Long-Term Fellowship from the European Molecular
324 Biology Organization (EMBO-LTF, ALTF 232-2016) and a Veni grant from the Netherlands Organization for
325 Scientific Research (016.VENI.171.097). G.v.d.B. is funded by a Young Investigator Grant from the Human

Frontier Science Program (HFSP; RGY0080/2018) and a Vidi grant from the Netherlands Organisation for Scientific Research (NWO-ALW VIDI 864.14.001). D.J.L. is funded by a Vidi grant (ZONMW VIDI 917.13.359), a ZONMW Medium Investment Grant (40-00506-98-9001) from the Netherlands Organisation for Scientific Research, and Erare grants EUROCDG2 and Euroglycanomics. K.Õ, M-A.V., S.P., and K.M. were supported by the Estonian Research Council grants GARLA8175, PUT355, PUTJD827 and PRG471.

Author Contributions

P.T.A.L., M.t.B., D.J.L., and G.v.d.B. designed the experiments and wrote the paper. E.C.F.G. contributed to the Stx5 kinetics, co-immunoprecipitation, and FLIM experiments. A.A., M.-A.V., M.B., F.Z., K.H., K.R., K.M., and K.Õ. contributed to the clinical data, exome sequencing and glycomics. O.F. and S.P. performed homozygosity mapping and prioritization of exome variants. N.H.R. performed TEM. R.A. contributed to the Stx5ΔL experiments. P.T.A.L. and M.t.B. performed all other experiments. All authors contributed to writing the manuscript.

Declaration of Interests

The authors declare that they have no competing financial interests.

Methods

Ethics

The study was approved by Research Ethics Committee of the University of Tartu (approval dates 19.12.2011, 20.02.2012 and 17.03.2014, and approval numbers 210/M-17, 212/M-31 and 235/M-13, 17.03.2014, respectively) and were strictly in accordance with the Declaration of Helsinki. Informed consent for carrying out research was obtained from the family of investigated individuals.

Glycosylation studies

Screening for Congenital Disorders of Glycosylation (CDG) was carried out as described before[62]. Plasma N-glycan profiling was performed by MALDI-TOF mass spectrometry of permethylated glycans[72], using 10 µL of plasma. High resolution mass spectrometry of intact transferrin was performed on a 6540 nanochip QTOF (Agilent), according to published protocols[73].

355

356 *Microarray analysis*

357 DNA was extracted either from peripheral blood according to the standard salting out protocol (IV:9 and IV-
358 :10) or from amnionic fluid cell culture (IV:8). Screening for chromosomal abnormalities was performed using
359 HumanCytoSNP-12 BeadChips (Illumina Inc., San Diego, CA, USA). 200 ng of total DNA per sample was
360 processed according to the protocol supplied by the manufacturer. Genotypes were called by GenomeStudio
361 v2011.1 software and the data were analyzed using GenomeStudio Genome Viewer tool (Illumina Inc.). The
362 minimum threshold for LCSH (long contiguous stretches of homozygosity) regions was set at 5 Mb.

363

364 *Exome sequencing*

365 Genomic DNA was extracted from fibroblasts from patient IV:9 according to the manufacturer's protocol using
366 a Qiagen Mini Kit (Qiagen) and was checked for DNA degradation on agarose gels. Next generation sequencing
367 (NGS) and analysis was performed as described[63]. In brief, exome enrichment was performed using the
368 SureSelect Human All Exon 50 Mb Kit (Agilent), covering ~21,000 genes. The exome library was sequenced on a
369 SOLiD 5500xl sequencer (Life Technologies). Color space reads were iteratively mapped to the hg19 reference
370 genome with the SOLiD LifeScope software version 2.1. Called variants and indels were annotated using an in-
371 house annotation pipeline[74,75] and common variants were filtered out based on a frequency of >0.5 % in
372 dbSNP and a frequency of >0.3 % in our in-house database of >5,000 exomes. Quality criteria were applied to
373 filter out variants with less than 5 variant reads and less than 20 % variation. Furthermore, synonymous
374 variants, deep intronic, intergenic and UTR variants were excluded. The identified variant was confirmed by
375 Sanger sequencing in all affected individuals (IV:8, IV:9, and IV:10) and their mother (III:2). Paternal DNA (III:1)
376 was not available.

377

378 *Cell culture*

379 HeLa cells (authenticated by ATCC through their human STR profiling cell authentication service), including
380 Stx5ΔL cell lines, were maintained in high glucose DMEM with Glutamax (Gibco 31966021). Human primary
381 dermal fibroblasts were obtained from patients or healthy donors and maintained in Medium 199 with EBSS
382 and L-glutamine (Lonza BE12-119F). All media were supplemented with 10% fetal calf serum (FCS, Greiner Bio-

one, Kremsmünster, Austria) and antibiotic-antimycotic solution (Gibco 15240-062). All cells were regularly tested for mycoplasma contamination.

Plasmids and transfection

Str-KDEL_ManII-SBP-EGFP was a gift from Franck Perez (Addgene plasmid #65252; http://n2t.net/addgene:65252; RRID:Addgene_65252). VAMP8-mCherry was constructed earlier[36] and previously deposited to Addgene (Addgene plasmid #92424). Str-KDEL_Stx5L-SBP-mCitrine and Str-KDEL_Stx5S-SBP-mCitrine were constructed by replacing the ManII-SBP-EGFP cassette in Str-KDEL_ManII-SBP-EGFP using the AscI and XbaI restriction sites. Stx5 coding sequences were codon-optimized for *Homo sapiens* using JCat and ordered from Genscript. Stx5LΔER coding sequence was generated with Q5-polymerase site-directed mutagenesis, using the Stx5L cDNA as a template with the following primer: 5'- CTTCG AATTC AATGA TTCCG GCCGC CGCCT ACGGC AGCAA GAACA CC. Sequences were verified with Sanger sequencing. HeLa cells were transfected with plasmid vectors using Fugene HD (Promega E2311), using the recommended protocol of the manufacturer. Only cells expressing low to moderate levels of the transfected plasmids, based on fluorescence intensity and manual localization scoring, were chosen for subsequent microscopic analyses.

CRISPR/Cas9

Stable knock out of Stx5L in HeLa cells was obtained using the CRISPR-CAS9 method. For this, pairs of gRNA sequences were designed upstream of the STX5 initiation codon (crispr.mit.edu, pair 1: ATAAC CTCGG ACTGT TGTGG AGG and ATGAT CCCGC GGAAA CGCTA CGG; pair 2: TAACC TCGGA CTGTT GTGGA GGG and TGATC CCGCG GAAAC GCTAC GGG). The gRNA sequences were cloned in pSpCas9n(BB)-2A-Puro (PX462) V2.0 (gift from Feng Zhang, Addgene no. 62987)[76] and transfected into HeLa cells by electroporation (Neon Transfection System, Thermofisher, MA). After initial selection with puromycin, the medium was changed for conditioned medium (collected from wildtype HeLa cells at 70% confluency) supplemented 1:1 with fresh medium. Single clones were obtained and screened for knockout of Stx5L by SDS-PAGE and Western blotting. Two clones (B1A7 and C1F4) were chosen for further experiments.

411 *Immunofluorescence*

412 Cells were plated on cleaned 12 mm glass coverslips (Electron Microscopy Services, 72230-01) and the
413 following day fixed with 4% paraformaldehyde for 15 minutes at room temperature. Following quenching with
414 50 mM NH_4Cl in PBS, cells were permeabilized and blocked in 2% normal donkey serum (Rockland, 017-000-
415 121) and 0.1% saponin (permeabilization buffer) for 30 mins at RT. Primary and secondary antibodies (list of
416 antibodies and dilutions in Supplementary Table 5) were diluted in permeabilization buffer and incubated for 1
417 hour at room temperature. Finally, cells were washed with 0.1% Triton X-100 in PBS to remove background
418 staining and mounted with mounting medium containing 0.01% Trolox (6-hydroxy-2,5,7,8-
419 tetramethylchroman-2-carboxylic acid) and 68% glycerol in 200 mM sodium phosphate buffer at pH 7.5 with
420 0.1 µg/ml DAPI. Coverslips were sealed with nail polish. Cells were imaged on a Leica SP8 SMD confocal laser
421 scanning microscope, equipped with an HC PL APO CS2 63x/1.20 WATER objective.
422
423 *Lectin stainings*
424 Cells were plated on cleaned 12 mm glass coverslips and after 72 hours culturing fixed with 4%
425 paraformaldehyde. Cells were blocked with Carbo-Free Blocking solution (Vector Laboratories, SP-5040) and
426 incubated with 4 µg/mL biotinylated SNA-I (Vector Laboratories, B-1305) or PNA (Vector Laboratories, B-1075)
427 diluted in Carbo-Free Blocking solution. Cells were then incubated with Streptavidin-Alexa Fluor 647
428 (ThermoScientific, S32357) before coverslips were mounted as described above. Cells were imaged on a Leica
429 SP8 SMD confocal laser scanning microscope, equipped with an HC PL APO CS2 63x/1.20 WATER objective.
430
431 *Brefeldin A assay*
432 Fibroblasts were plated in black clear-bottom 96-wells plates (Greiner, 655090) and cultured until 80%
433 confluent. Cells were either treated with 10 µg/mL Brefeldin A in DMSO (Cayman Chemicals, 11861) or DMSO
434 alone for 15 minutes in a humified incubator. After incubation, plates were transferred immediately to ice and
435 cells were fixed with 4% paraformaldehyde, after which the above immunofluorescence protocol was
436 performed. Microscopy images were acquired using a Leica high-content microscopy system based on a Leica
437 DMI6000B (Leica Microsystems) and an HCX PL S-APO 40.0x0.75 DRY objective. HeLa cells were plated on 12
438 mm coverslips and incubated in the same way with Brefeldin A, but fixed with 100% methanol at -20°C for 15
439 mins. Imaging of these samples was performed using a Leica DMI6000B epifluorescence microscope equipped

with an HC PL APO 63x1.40 OIL objective. Cells were analyzed using Fiji (http://fiji.sc/) by first removing noise outliers (bright outliers, radius 2.0 pixels, threshold 50), then manually selecting cells and measuring the maximum fluorescence intensity in these ROIs. Data were normalized to the mean of the DMSO control of each group.

H-89 assay

HeLa cells were plated on 12 mm coverslips and incubated the following day for 30 mins with 100 µM H-89 (Cayman Chemicals, 10010556) in DMSO or DMSO alone (vehicle) and H-89 was washed out with fresh medium for 5 mins. Cells were fixed with 4% paraformaldehyde for 15 mins at RT and permeabilized with 100% methanol at -20°C for 15 mins prior to immunostaining with ERGIC53 mouse monoclonal antibody (G1/93 or OTI1A8) before epifluorescence imaging as described for the BFA assay. Cells were analyzed using Fiji and the number of ERGIC53-positive spots was quantified with the Spot Counter plugin. Data were normalized to the mean fluorescence of the DMSO control of each group. Data was analyzed with a Mann-Whitney U non-parametric test.

Transmission electron microscopy

Fibroblasts were grown in 12-wells plates and fixed with 2% glutaraldehyde (Sigma-Aldrich, G5882) in PB (0.1 M phosphate buffer, pH 7.4) for 60 mins at room temperature. Subsequently, cells were washed four times with PB and post-fixed with 1% osmium tetroxide and 1% potassium ferrocyanide in PB for 60 mins at room temperature. Then, cells were again washed four times with PB and dehydrated with graded steps of ethanol (30%, 50%, 70%, 96%, 100%) and embedded in Epon resin. 70 nm sections were cut with an ultramicrotome, then stained with 2% uranyl acetate solution and lead citrate solution. Stained sections were then examined using a JEOL JEM1400 transmission electron microscope.

Live-cell epifluorescence microscopy

Cells were seeded in four-compartment dishes (Greiner 627870) and transfected as described above (3:1 weight ratio reporter construct:Golgi label). Briefly before imaging, the culture medium was exchanged for Leibovitz's L-15 (Gibco 21083027). Samples were imaged using a DMI6000B (Leica Microsystems) with a heated stage (Pecon) and objective heater. All samples were imaged using an HC PL APO 63x/1.40–0.60 OIL

469 objective. VSVG-ts045-EGFP experiments were performed at 32°C after overnight incubation at 40°C, while all
470 other epifluorescence experiments were performed at 37°C. For RUSH experiments, an equal amount of
471 Leibovitz's L-15 supplemented with biotin was added to the well immediately before imaging, to reach a final
472 concentration of 40 µM biotin. Live cell imaging was started immediately with 15 sec or 30 sec frame rates.
473 Analysis was performed with Fiji, after registration of the image stacks, the increase in fluorescence was
474 measured in the Golgi area by using the thresholded mScarlet-Giantin signal as an image mask.
475
476 *FRET-FLIM*
477 All imaging took place in Leibovitz's L-15 supplemented with 10 µg/mL cycloheximide (Sigma-Aldrich, C4859)
478 and cells were pulsed with biotin as described above. Imaging was performed on a Leica SP8 SMD system at
479 37°C, equipped with an HC PL APO CS2 63x/1.20 WATER objective. Fluorophores were excited with a pulsed
480 white light laser, operating at 80 MHz. mCitrine was excited at 514 nm, two separate HyD detectors were used
481 to collect photons, set at 521-565 nm and 613-668 nm respectively. Photons were collected for one minute
482 and lifetime histograms of the donor fluorophore were fitted with monoexponential decay functions
483 convoluted with the microscope instrument response function in Leica LAS X.
484 *Immunoprecipitation*
485 HeLa cells were lysed 48 hours post-transfection with IP lysis buffer (20 mM Tris-HCl pH 7.6, 137 mM NaCl, 1%
486 IGEPAL, 2 mM EDTA and complete protease inhibitors (Roche 5892791001)). Protein levels were equilibrated
487 and lysates were immunoprecipitated with 1 µg anti-GFP-antibody (Rockland 600-401-215) and protein A
488 beads (ThermoFisher, 20333) for 1 hour at 4°C with constant agitation. After three washes with IP lysis buffer,
489 samples were boiled in 5x SDS sample buffer with β-mercaptoethanol and resolved with SDS-PAGE and
490 subsequent immunoblotting.
491
492 *SDS-PAGE and immunoblotting*
493 Cells were plated in 12-wells plates in culture medium and lysed the following day with SDS lysis buffer (1%
494 SDS, 10 mM Tris-HCl pH 6.8). Lysates were diluted to equal protein content (30 µg per lane) with SDS lysis
495 buffer, separated with SDS-PAGE on 4–20% Mini-PROTEAN TGX Precast Protein Gels (Biorad, 4561094) and
496 subsequently transferred onto 0.45 µm PVDF membranes. Small molecular weight proteins (Bet1 and Bet1L)
497 were separated on 16% Schaegger gels[77].

Quantification and statistical analysis

All mean values represent the average of all cells analyzed. All comparisons between two groups were first checked for similar mean and median values and acceptable (< 3x) difference in variance, before statistical analysis with an unpaired two-sided Student's t-test. Relative intensity data was first transformed using the binary logarithm before analysis with an unpaired two-sided Student's t-test. H-89 data was analyzed with a Mann-Whitney U non-parametric test. Stx5 kinetics data were analyzed with a one-way ANOVA, followed by a posthoc Tukey's honestly significant difference test. Stx5 FLIM data were analyzed with a two-way ANOVA, with the isoform and timepoint as independent variables, followed by a posthoc Tukey's honestly significant difference test. $p < 0.05$ was considered significant. *$p < 0.05$, **$p < 0.01$, ***$p < 0.001$, ****$p \leq 0.0001$. All statistical analyses were performed using R statistical software. All numerical data were visualized using R package *ggplot2*[78], with violins representing the overall distribution of the data and means ± 95% CI overlaid.

Data and code availability

Microarray data, exome sequencing data and ImageJ macros for quantification of the RUSH experiments are available upon request.

514 **Figures**

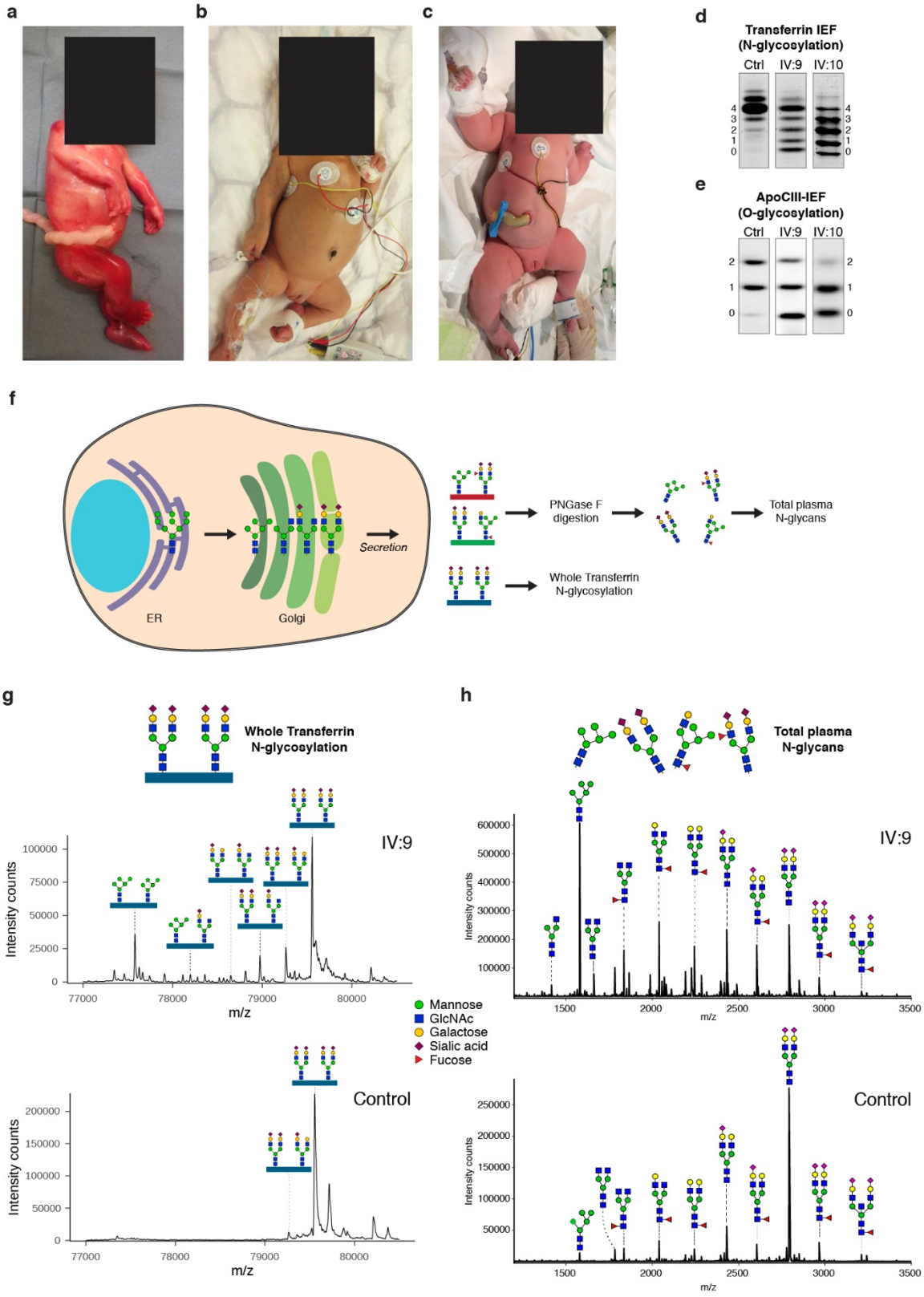

Figure 1. A novel, lethal, genetic variant suggests a defect in protein glycosylation related to Golgi trafficking.

(a-c) Clinical images of Stx5M55V patients IV:8 (a), IV:9 (b), IV:10 (c).

(d) Glycosylation screening by isoelectric focusing (IEF) of serum transferrin. The accompanying numbers represent the total number of sialic acids in the different proteoforms. Both patients show a reduction in the number of sialic acids.

(e) Glycosylation screening by IEF of serum Apolipoprotein C3 (ApoCIII). ApoCIII has one mucin-type O-linked glycan with one or two sialic acids in controls. Both patients show a reduction in the number of sialic acids.

(f) Schematic overview of N-glycosylation intermediates in the Golgi. For mass spectrometry analysis of glycan structures, glycosylated transferrin is enriched from all secreted glycoproteins in human serum and subjected to intact protein mass spectrometry. In parallel, a different serum sample is treated with PNGase F to cleave and analyze N-glycans from all plasma proteins.

(g) Nanochip-C8 QTOF mass spectra of enriched intact serum Transferrin of Stx5M55V patient IV:9 (top spectrum) and healthy control (lower spectrum) are shown. Key transferrin glycoforms are shown, indicating a strong increase of high-mannose glycans and glycans lacking sialic acid and galactose. Annotation of all peaks of patients IV:9 and IV:10 is shown in Supplementary Table 2.

(h) MALDI-TOF mass spectra of total plasma N-glycans of Stx5M55V patient IV:9 (top spectrum) and healthy control (lower spectrum) are shown. Structural analysis shows a strong increase of high-mannose glycans and glycans lacking sialic acid and galactose. Annotation of all peaks of patients IV:9 and IV:10 is shown in Supplementary Table 3.

536

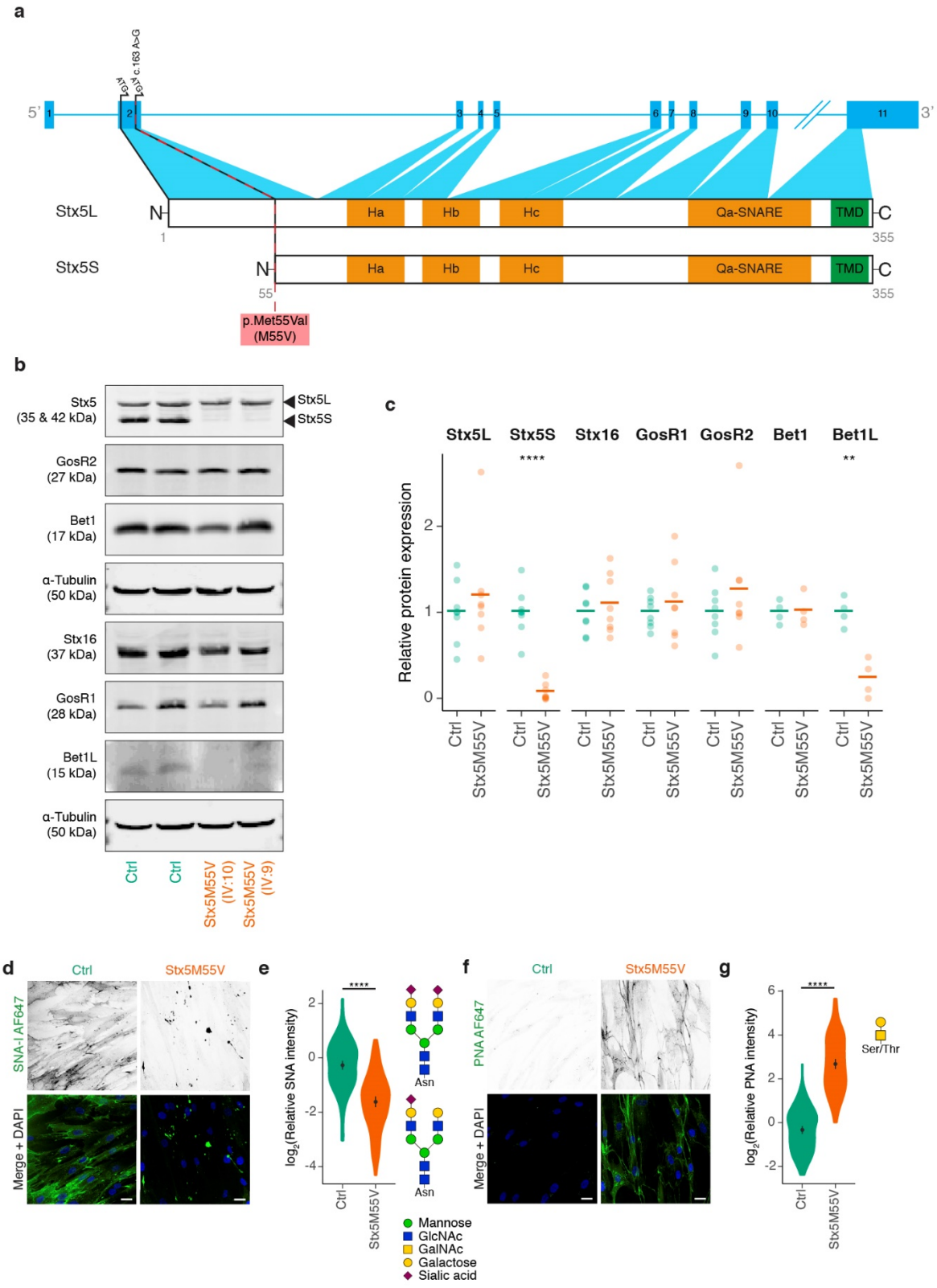

537

Figure 2. Primary dermal fibroblasts are an accurate model of the glycosylation defect observed in Stx5M55V patients.

(a) Schematic representation of the intron-exon structure of *STX5* and the encoded proteoforms resulting from the two starting codons in exon 2. The Stx5M55V genetic variant is indicated by a dashed red line. Orange regions have a secondary helical structure. TMD, transmembrane domain. Ha, Hb, Hc: regulatory Habc-domain (b) Representative immunoblot for SNARE proteins of cell lysates of primary human dermal fibroblasts of healthy donors (green, Ctrl) or Stx5M55V patients (orange, Stx5M55V). α-Tubulin, loading control.

(c) Quantification of (b). Protein levels were first normalized to the loading control, then to the average expression of both control lines. Each point represents one cell line from 2 independent experiments.

(d) Fibroblasts of healthy donors (green, Ctrl) or Stx5M55V patients (orange, Stx5M55V) were probed with SNA-I lectin (green in merge). Representative confocal micrographs. Scalebars, 25 µm. DAPI in blue.

(e) Quantification of (d). All data were normalized to the healthy donor and then $\log_2$-transformed. N = 124 (Ctrl) and 111 (Stx5M55V) cells from 2 independent experiments.

(f-g) Same as panels (d-e), but now for PNA lectin. N = 117 (Ctrl) and 122 (Stx5M55V) cells from 2 independent experiments.

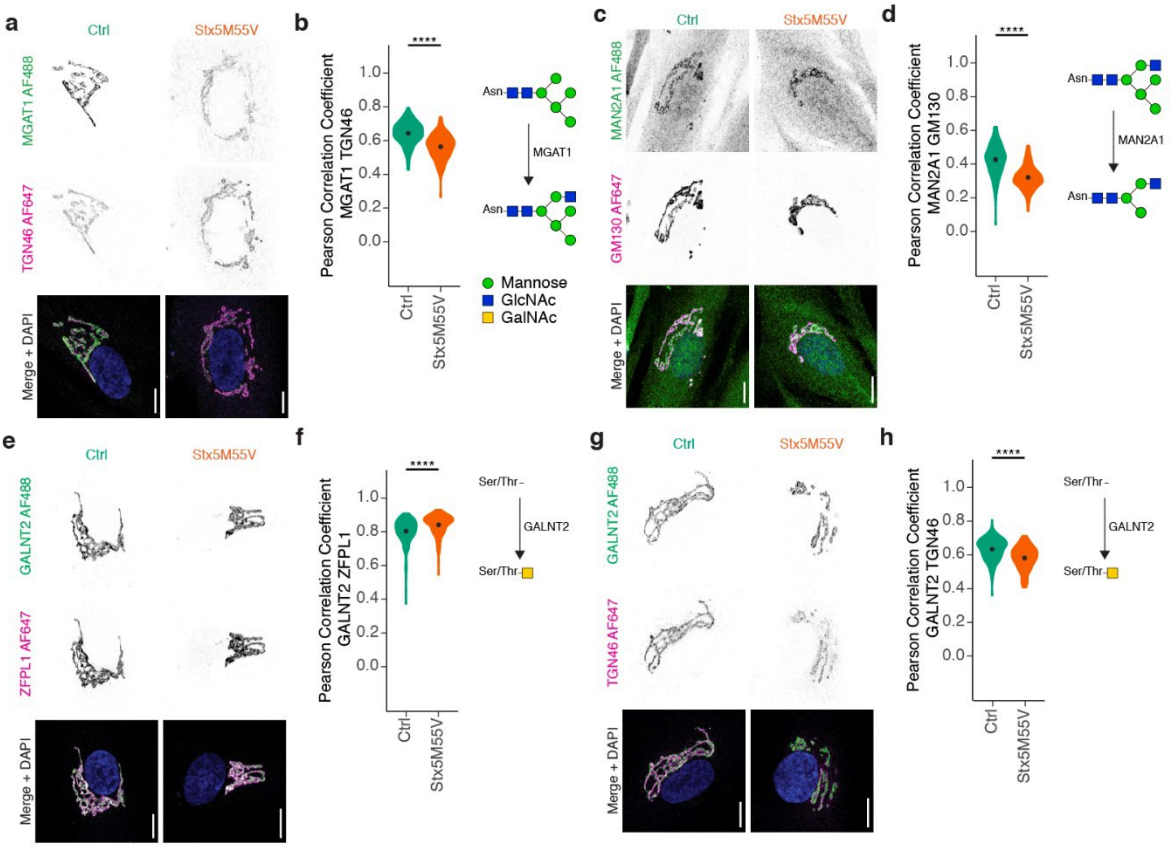

554

555 **Figure 3. Glycosylation enzymes mislocalize in Stx5M55V patient fibroblasts.**

556 (a) Immunofluorescence microscopy of MGAT1 (green in merge) and TGN46 (magenta) in primary dermal

557 fibroblasts of healthy donors (green, Ctrl) or Stx5M55V patients (orange, Stx5M55V). Representative confocal

558 micrographs. Scalebars, 10 µm. DAPI in blue.

559 (b) Pearson's correlations coefficients between MGAT1 and TGN46 of panel (a). N = 157 (Ctrl) and 162

560 (Stx5M55V) cells from 2 independent experiments.

561 (c-d) Same as panels (a-b), but now for MAN2A1 (green) and GM130 (magenta). N = 127 (Ctrl) and 143

562 (Stx5M55V) cells from 2 independent experiments.

563 (e-f) Same as panels (a-b), but now for GALNT2 (green) and ZFPL1 (magenta). N = 240 (Ctrl) and 146

564 (Stx5M55V) cells from 2 independent experiments.

565 (g-h) Same as panels (a-b), but now for GALNT2 (green) and TGN46 (magenta). N = 172 (Ctrl) and 152

566 (Stx5M55V) cells from 2 independent experiments.

567

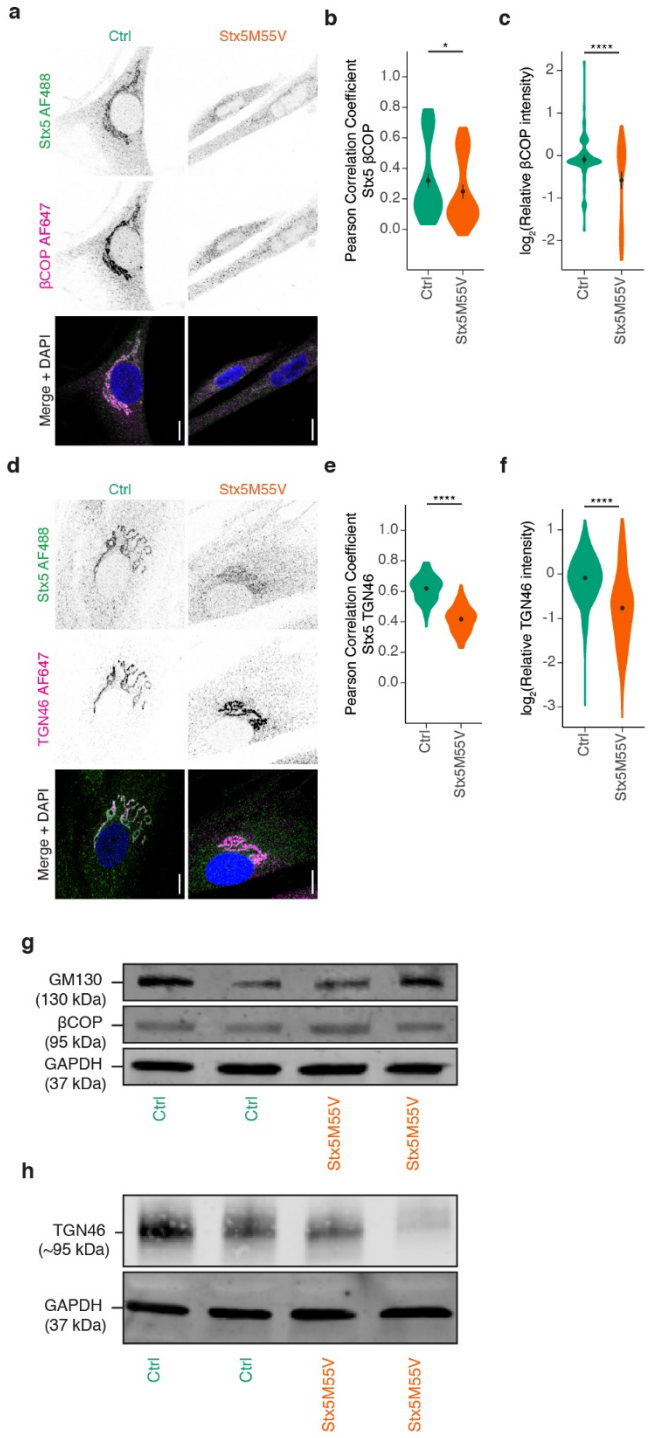

568 **Figure 4. Reduced localization of Stx5 to trans-Golgi network in Stx5M55V patients.**

569 (a) Immunofluorescence microscopy of Stx5 (green in merge) and βCOP (magenta) in primary dermal

570 fibroblasts of healthy donors (green, Ctrl) or Stx5M55V patients (orange, Stx5M55V). Representative confocal

571 micrographs. Scalebars, 10 µm. DAPI in blue.

572 (b) Pearson's correlations coefficients between Stx5 and βCOP of panel (a). N = 109 (Ctrl) and 87 (Stx5M55V)

573 cells from 2 independent experiments.

574 (c) Fluorescence intensities of βCOP from panel (a) relative to the healthy control. N = 109 (Ctrl) and 87

575 (Stx5M55V) cells from 2 independent experiments.

576 (d-f) Same as panels (a-c), but now for Stx5 (green) and TGN46 (magenta). N = 128 (Ctrl) and 114 (Stx5M55V)

577 cells from 2 independent experiments for colocalization, N = 822 (Ctrl) and 783 (Stx5M55V) cells from 6

578 independent experiments for intensity.

579 (g) Representative immunoblot for GM130 and βCOP of the cells from panel A. GAPDH, loading control.

580 (h) Same as panel (g), but now for TGN46.

581

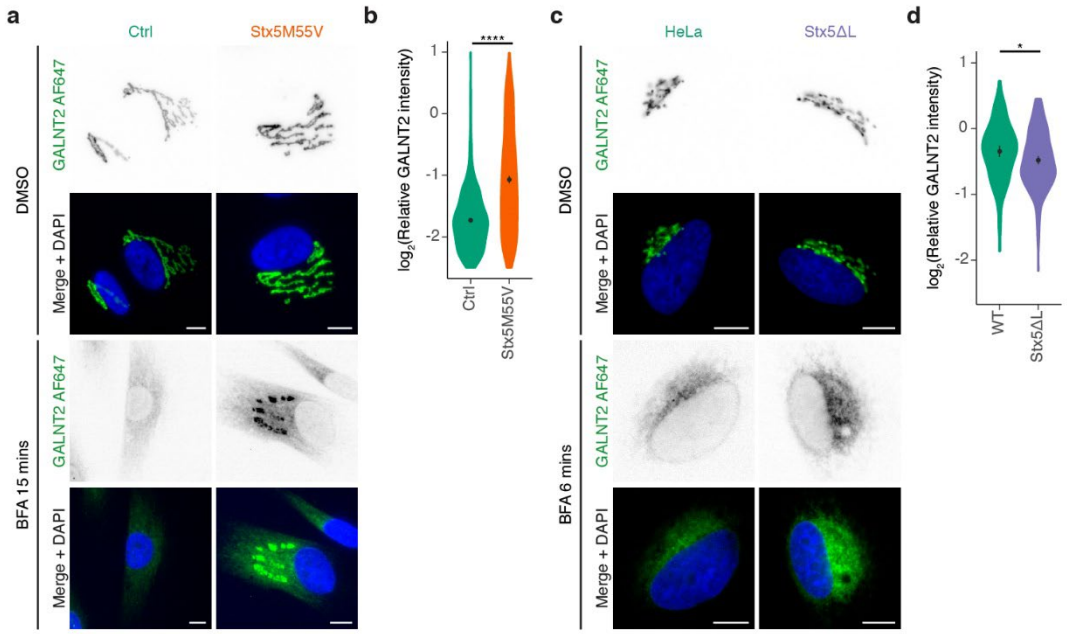

582 **Figure 5. Loss of Stx5S inhibits ER-Golgi trafficking, while the loss of Stx5L accelerates ER-Golgi trafficking.**

583 (a) Immunofluorescence microscopy of GALNT2 (green in merge) in primary human dermal fibroblasts of
584 healthy donors (green, Ctrl) or Stx5M55V patients (orange, Stx5M55V) in the absence or presence of Brefeldin
585 A (BFA) for 15 min. Representative epifluorescence micrographs are shown. Scalebars, 10 µm. DAPI in blue.
586 (b) Relative maximum fluorescence intensities of GALNT2 from panel (A). All data were normalized to the
587 DMSO condition (vehicle). N = 979 (Ctrl) and 943 (Stx5M55V) cells from 2 independent experiments.

588 (c-d) Same as panels (a-b) B, but now in parental HeLa and Stx5ΔL lines with only 6 min BFA treatment. N = 103
589 (WT) and 212 (Stx5ΔL) cells from 2 independent experiments.

590

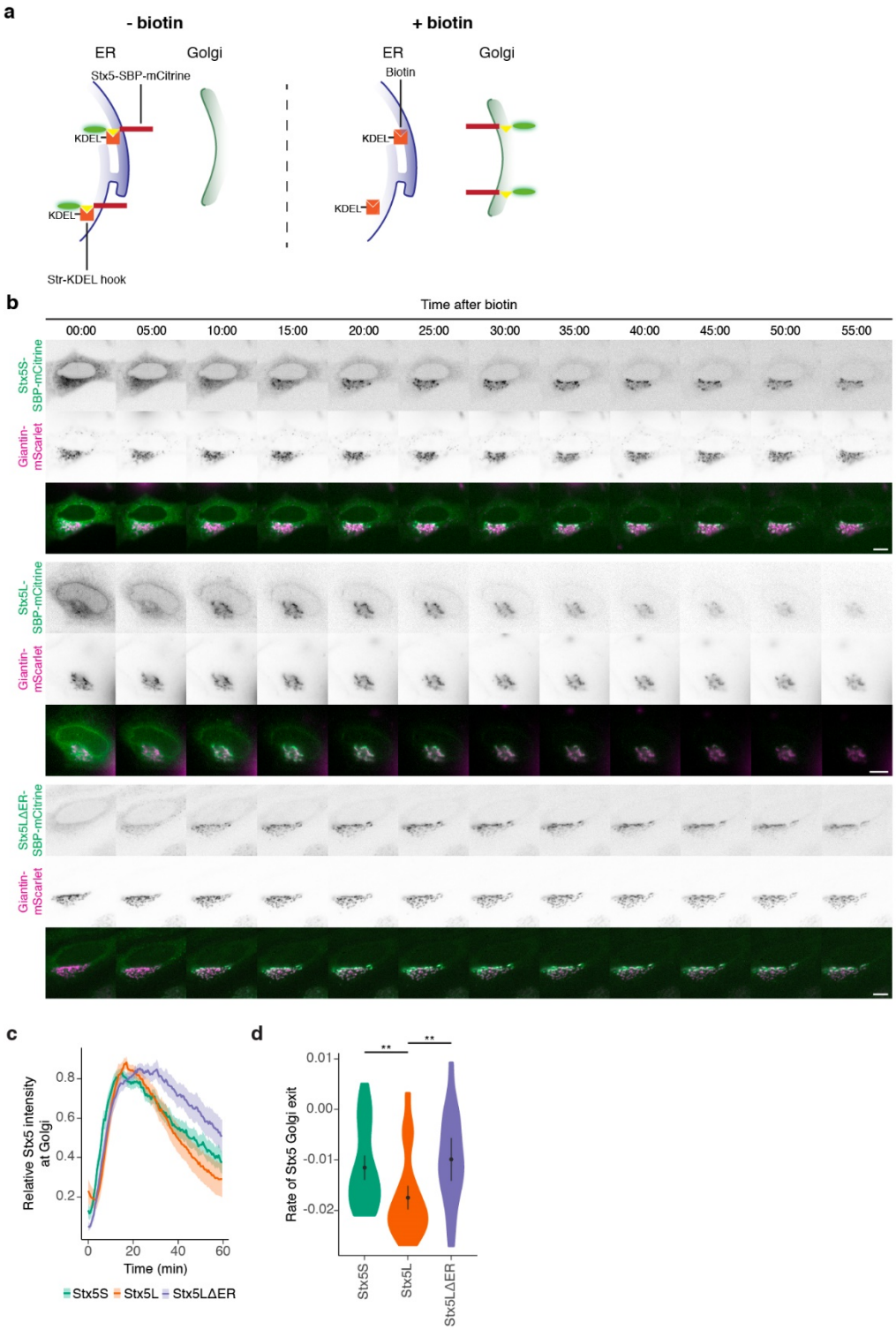

591 **Figure 6. Faster Golgi transit of Stx5L than Stx5S**

592 (a) Schematic overview of the design of Stx5 trafficking experiment, based on the RUSH system. In absence of

593 biotin (left panel), the reporter cargo (Stx5-SBP-mCitrine) is trapped at the ER by the lumenal Str-KDEL hook.

When biotin is added (right panel), biotin outcompetes the interaction with streptavidin, allowing Stx5-SBP-mCitrine to traffic freely to its destination compartment. SBP, streptavidin binding protein; Str, streptavidin. (b) Snapshots of live-cell imaging of Stx5-SBP-mCitrine (green in merge). Magenta: Golgi marker Giantin-mScarlet. Scale bars, 10 µm. See also supplementary movies 5 – 7.

(c) Quantification of mCitrine fluorescence at the Golgi of Stx5S-SBP-mCitrine (green), Stx5L-SBP-mCitrine (orange) and Stx5LΔER-SBP-mCitrine (blue) over time from panel (b). N = 44 (Stx5S), 47 (Stx5L) and 19 (Stx5ΔER) cells from 4 independent experiments.

(d) Quantification of the slopes from panel (c) of the post-Golgi section (~20 mins onwards).

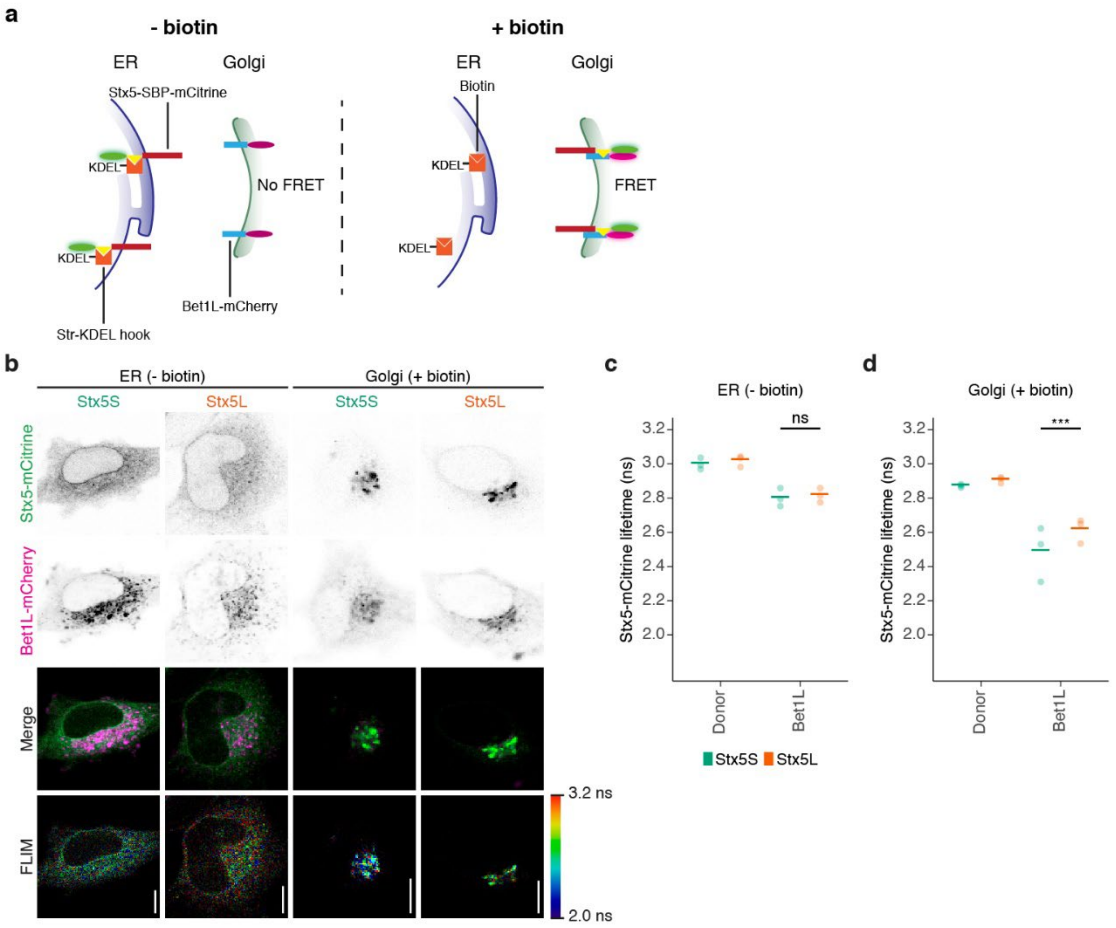

Figure 7. Stx5S is the dominant Qa-SNARE for intra-Golgi trafficking

(a) Schematic overview of experimental design for complex formation of Stx5 isoforms with Bet1L, based on the RUSH system and SNARE complex measurement by FRET-FLIM. In absence of biotin (left panel), the reporter cargo (Stx5-SBP-mCitrine) is trapped at the ER by the lumenal Str-KDEL hook, and no FRET with Golgi-localized Bet1L-mCherry can occur. When biotin is added (right panel), biotin outcompetes the interaction with streptavidin, allowing Stx5-SBP-mCitrine to traffic freely to its destination compartment, and SNARE complex formation with Golgi-localized Bet1L-mCherry can occur resulting in FRET. SBP, streptavidin binding protein; Str, streptavidin; FRET, Förster resonant energy transfer. FLIM, fluorescence lifetime imaging microscopy.

(b) Representative confocal micrographs of HeLa cells co-expressing Stx5-mCitrine (green in merge) and Bet1L-mCherry (magenta) without (ER) or with (Golgi) biotin. Scalebars, 10 µm.

(c-d) Average fluorescence lifetimes at the ER (c) and Golgi (d) from panel (b). N = 52 (Stx5S Donor ER), 74 (Stx5L Donor ER), 47 (Stx5S Bet1L ER), 51 (Stx5L Bet1L ER), 50 (Stx5S Donor Golgi), 71 (Stx5L Donor Golgi), 58

(Stx5S Bet1L Golgi) and 58 (Stx5L Bet1L Golgi) cells from 3 independent experiments. Each point represents one independent experiment.

References

1. Bentley, M. *et al.* SNARE status regulates tether recruitment and function in homotypic COPII vesicle fusion. *The Journal of biological chemistry* **281**, 38825–33 (2006).
2. Dascher, C., Matteson, J. & Balch, W. E. Syntaxin 5 regulates endoplasmic reticulum to Golgi transport. *The Journal of biological chemistry* **269**, 29363–6 (1994).
3. Rowe, T., Dascher, C., Bannykh, S., Plutner, H. & Balch, W. E. Role of vesicle-associated syntaxin 5 in the assembly of pre-Golgi intermediates. *Science (New York, N.Y.)* **279**, 696–700 (1998).
4. Xu, D., Joglekar, A. P., Williams, A. L. & Hay, J. C. Subunit structure of a mammalian ER/Golgi SNARE complex. *The Journal of biological chemistry* **275**, 39631–9 (2000).
5. Hay, J. C. *et al.* Localization, Dynamics, and Protein Interactions Reveal Distinct Roles for ER and Golgi SNAREs. *The Journal of Cell Biology* **141**, 1489–1502 (1998).
6. Paek, I. *et al.* ERS-24, a Mammalian v-SNARE Implicated in Vesicle Traffic between the ER and the Golgi. *The Journal of Cell Biology* **137**, 1017–1028 (1997).
7. Zhang, T. *et al.* Ykt6 forms a SNARE complex with syntaxin 5, GS28, and Bet1 and participates in a late stage in endoplasmic reticulum-Golgi transport. *The Journal of biological chemistry* **276**, 27480–7 (2001).
8. Jahn, R. & Scheller, R. H. SNAREs — engines for membrane fusion. *Nature Reviews Molecular Cell Biology* **7**, 631–631 (2006).
9. Banfield, D. K., Lewis, M. J. & Pelham, H. R. B. A SNARE-like protein required for traffic through the Golgi complex. *Nature* **375**, 806–809 (1995).
10. Parlati, F. *et al.* Topological restriction of SNARE-dependent membrane fusion. *Nature* **407**, 194–198 (2000).
11. Parlati, F. *et al.* Distinct SNARE complexes mediating membrane fusion in Golgi transport based on combinatorial specificity. *Proceedings of the National Academy of Sciences of the United States of America* **99**, 5424–9 (2002).
12. Xu, Y., Martin, S., James, D. E. & Hong, W. GS15 Forms a SNARE Complex with Syntaxin 5, GS28, and Ykt6 and Is Implicated in Traffic in the Early Cisternae of the Golgi Apparatus. *MBoC* **13**, 3493–3507 (2002).
13. Linders, P. T., van der Horst, C., ter Beest, M. & van den Bogaart, G. Stx5-Mediated ER-Golgi Transport in Mammals and Yeast. *Cells* **8**, 780 (2019).

14. Malsam, J. & Söllner, T. H. Organization of SNAREs within the Golgi stack. *Cold Spring Harbor perspectives in biology* **3**, a005249–a005249 (2011).
15. Tai, G. *et al.* Participation of the Syntaxin 5/Ykt6/GS28/GS15 SNARE Complex in Transport from the Early/Recycling Endosome to the Trans-Golgi Network. *MBoC* **15**, 4011–4022 (2004).
16. Dickinson, M. E. *et al.* High-throughput discovery of novel developmental phenotypes. *Nature* **537**, 508–514 (2016).
17. Koscielny, G. *et al.* The International Mouse Phenotyping Consortium Web Portal, a unified point of access for knockout mice and related phenotyping data. *Nucleic Acids Res* **42**, D802–D809 (2014).
18. Hui, N. *et al.* An isoform of the Golgi t-SNARE, syntaxin 5, with an endoplasmic reticulum retrieval signal. *Molecular biology of the cell* **8**, 1777–87 (1997).
19. Gao, G. & Banfield, D. K. Multiple features within the syntaxin Sed5p mediate its Golgi localization. *Traffic* **21**, 274–296 (2020).
20. Dominguez, M. *et al.* gp25L/emp24/p24 protein family members of the cis-Golgi network bind both COP I and II coatomer. *The Journal of cell biology* **140**, 751–65 (1998).
21. Miyazaki, K. *et al.* Contribution of the long form of syntaxin 5 to the organization of the endoplasmic reticulum. *Journal of Cell Science* **125**, 5658 LP – 5666 (2012).
22. Suga, K., Saito, A., Tomiyama, T., Mori, H. & Akagawa, K. The Syntaxin 5 Isoforms Syx5 and Syx5L have Distinct Effects on the Processing of β-amyloid Precursor Protein. *The Journal of Biochemistry* **146**, 905–915 (2009).
23. Avci, D. *et al.* The intramembrane protease SPP impacts morphology of the endoplasmic reticulum by triggering degradation of morphogenic proteins. *J. Biol. Chem.* **294**, 2786–2800 (2019).
24. Hay, J. C., Hirling, H. & Scheller, R. H. Mammalian vesicle trafficking proteins of the endoplasmic reticulum and Golgi apparatus. *J. Biol. Chem.* **271**, 5671–5679 (1996).
25. Shestakova, A., Suvorova, E., Pavliv, O., Khaidakova, G. & Lupashin, V. Interaction of the conserved oligomeric Golgi complex with t-SNARE Syntaxin5a/Sed5 enhances intra-Golgi SNARE complex stability. *The Journal of Cell Biology* **179**, 1179–1192 (2007).
26. Zhang, T. *et al.* The Mammalian Protein (rbet1) Homologous to Yeast Bet1p Is Primarily Associated with the Pre-Golgi Intermediate Compartment and Is Involved in Vesicular Transport from the Endoplasmic Reticulum to the Golgi Apparatus. *The Journal of Cell Biology* **139**, 1157–1168 (1997).

27. Mallard, F. *et al.* Early/recycling endosomes-to-TGN transport involves two SNARE complexes and a Rab6 isoform. *The Journal of Cell Biology* **156**, 653–664 (2002).

28. Dingjan, I. *et al.* Endosomal and Phagosomal SNAREs. *Physiological Reviews* **98**, 1465–1492 (2018).

29. Chiu, C.-F. *et al.* ZFPL1, a novel ring finger protein required for cis-Golgi integrity and efficient ER-to-Golgi transport. *The EMBO journal* **27**, 934–47 (2008).

30. Jaiman, A. & Thattai, M. Algorithmic biosynthesis of eukaryotic glycans. *bioRxiv* 440792 (2018) doi:10.1101/440792.

31. Glick, B. S. & Nakano, A. Membrane Traffic Within the Golgi Apparatus. *Annual Review of Cell and Developmental Biology* **25**, 113–132 (2009).

32. Galea, G., Bexiga, M. G., Panarella, A., O'Neill, E. D. & Simpson, J. C. A high-content screening microscopy approach to dissect the role of Rab proteins in Golgi-to-ER retrograde trafficking. *J Cell Sci* **128**, 2339–2349 (2015).

33. Boncompain, G. *et al.* Synchronization of secretory protein traffic in populations of cells. *Nature Methods* **9**, 493–493 (2012).

34. Lippincott-Schwartz, J., Roberts, T. H. & Hirschberg, K. Secretory Protein Trafficking and Organelle Dynamics in Living Cells. *Annual Review of Cell and Developmental Biology* **16**, 557–589 (2000).

35. Bindels, D. S. *et al.* mScarlet: a bright monomeric red fluorescent protein for cellular imaging. *Nature Methods* **14**, 53–56 (2017).

36. Verboogen, D. R. J., González Mancha, N., ter Beest, M. & van den Bogaart, G. Fluorescence Lifetime Imaging Microscopy reveals rerouting of SNARE trafficking driving dendritic cell activation. *eLife* **6**, (2017).

37. Griesbeck, O., Baird, G. S., Campbell, R. E., Zacharias, D. A. & Tsien, R. Y. Reducing the Environmental Sensitivity of Yellow Fluorescent Protein MECHANISM AND APPLICATIONS. *J. Biol. Chem.* **276**, 29188–29194 (2001).

38. Casey, J. R., Grinstein, S. & Orlowski, J. Sensors and regulators of intracellular pH. *Nature reviews. Molecular cell biology* **11**, 50–61 (2010).

39. Antonin, W., Holroyd, C., Tikkanen, R., Höning, S. & Jahn, R. The R-SNARE Endobrevin/VAMP-8 Mediates Homotypic Fusion of Early Endosomes and Late Endosomes. *MBoC* **11**, 3289–3298 (2000).

40. Bajno, L. *et al.* Focal Exocytosis of Vamp3-Containing Vesicles at Sites of Phagosome Formation. *J Cell Biol* **149**, 697–706 (2000).

41. Hong, W. SNAREs and traffic. *Biochimica et Biophysica Acta (BBA) - Molecular Cell Research* **1744**, 120–144 (2005).
42. Manderson, A. P., Kay, J. G., Hammond, L. A., Brown, D. L. & Stow, J. L. Subcompartments of the macrophage recycling endosome direct the differential secretion of IL-6 and TNFα. *J Cell Biol* **178**, 57–69 (2007).
43. Murray, R. Z. A Role for the Phagosome in Cytokine Secretion. *Science* **310**, 1492–1495 (2005).
44. Amberger, J. S., Bocchini, C. A., Schiettecatte, F., Scott, A. F. & Hamosh, A. OMIM.org: Online Mendelian Inheritance in Man (OMIM®), an online catalog of human genes and genetic disorders. *Nucleic Acids Res* **43**, D789–D798 (2015).
45. Pedersen, A. G. & Nielsen, H. Neural network prediction of translation initiation sites in eukaryotes: perspectives for EST and genome analysis. *Proc Int Conf Intell Syst Mol Biol* **5**, 226–233 (1997).
46. Kochetov, A. V. Alternative translation start sites and hidden coding potential of eukaryotic mRNAs. *BioEssays* **30**, 683–691 (2008).
47. Kozak, M. Regulation of translation via mRNA structure in prokaryotes and eukaryotes. *Gene* **361**, 13–37 (2005).
48. Oka, T., Ungar, D., Hughson, F. M. & Krieger, M. The COG and COPI Complexes Interact to Control the Abundance of GEARs, a Subset of Golgi Integral Membrane Proteins. *MBoC* **15**, 2423–2435 (2004).
49. Ohtsubo, K. & Marth, J. D. Glycosylation in Cellular Mechanisms of Health and Disease. *Cell* **126**, 855–867 (2006).
50. Freeze, H. H., Chong, J. X., Bamshad, M. J. & Ng, B. G. Solving Glycosylation Disorders: Fundamental Approaches Reveal Complicated Pathways. *The American Journal of Human Genetics* **94**, 161–175 (2014).
51. Fisher, P. & Ungar, D. Bridging the Gap between Glycosylation and Vesicle Traffic. *Front. Cell Dev. Biol.* **4**, (2016).
52. Blackburn, J. B., Kudlyk, T., Pokrovskaya, I. & Lupashin, V. V. More than just sugars: Conserved oligomeric Golgi complex deficiency causes glycosylation-independent cellular defects. *Traffic* **19**, 463–480 (2018).
53. Foulquier, F. *et al.* Conserved oligomeric Golgi complex subunit 1 deficiency reveals a previously uncharacterized congenital disorder of glycosylation type II. *PNAS* **103**, 3764–3769 (2006).
54. Foulquier, F. *et al.* A new inborn error of glycosylation due to a Cog8 deficiency reveals a critical role for the Cog1–Cog8 interaction in COG complex formation. *Hum Mol Genet* **16**, 717–730 (2007).

55. Kranz, C. *et al.* COG8 deficiency causes new congenital disorder of glycosylation type IIh. *Hum Mol Genet* **16**, 731–741 (2007).

56. Miller, V. J. & Ungar, D. Re'COG'nition at the Golgi. *Traffic* **13**, 891–897 (2012).

57. Morava, E. *et al.* A common mutation in the COG7 gene with a consistent phenotype including microcephaly, adducted thumbs, growth retardation, VSD and episodes of hyperthermia. *Eur J Hum Genet* **15**, 638–645 (2007).

58. Ng, B. G. *et al.* Molecular and clinical characterization of a Moroccan Cog7 deficient patient. *Molecular Genetics and Metabolism* **91**, 201–204 (2007).

59. Reynders, E. *et al.* Golgi function and dysfunction in the first COG4-deficient CDG type II patient. *Hum Mol Genet* **18**, 3244–3256 (2009).

60. Wu, X. *et al.* Mutation of the COG complex subunit gene COG7 causes a lethal congenital disorder. *Nat Med* **10**, 518–523 (2004).

61. Hucthagowder, V. *et al.* Loss-of-function mutations in ATP6V0A2 impair vesicular trafficking, tropoelastin secretion and cell survival. *Hum Mol Genet* **18**, 2149–2165 (2009).

62. Jansen, J. C. *et al.* CCDC115 Deficiency Causes a Disorder of Golgi Homeostasis with Abnormal Protein Glycosylation. *The American Journal of Human Genetics* **98**, 310–321 (2016).

63. Jansen, J. C. *et al.* TMEM199 Deficiency Is a Disorder of Golgi Homeostasis Characterized by Elevated Aminotransferases, Alkaline Phosphatase, and Cholesterol and Abnormal Glycosylation. *The American Journal of Human Genetics* **98**, 322–330 (2016).

64. Jansen, E. J. R. *et al.* ATP6AP1 deficiency causes an immunodeficiency with hepatopathy, cognitive impairment and abnormal protein glycosylation. *Nature Communications* **7**, 11600–11600 (2016).

65. Foulquier, F. *et al.* TMEM165 Deficiency Causes a Congenital Disorder of Glycosylation. *The American Journal of Human Genetics* **91**, 15–26 (2012).

66. Ashikov, A. *et al.* Integrating glycomics and genomics uncovers SLC10A7 as essential factor for bone mineralization by regulating post-Golgi protein transport and glycosylation. *Hum Mol Genet* **27**, 3029–3045 (2018).

67. Park, J. H. *et al.* SLC39A8 Deficiency: A Disorder of Manganese Transport and Glycosylation. *The American Journal of Human Genetics* **97**, 894–903 (2015).

762 68. Witkos, T. M. *et al.* GORAB scaffolds COPI at the trans -Golgi for efficient enzyme recycling and correct
763 protein glycosylation. *Nat Commun* **10**, 1–18 (2019).
764 69. Zhong, W. Golgi during Development. *Cold Spring Harb Perspect Biol* **3**, (2011).
765 70. Zhao, H. Membrane Trafficking in Osteoblasts and Osteoclasts: New Avenues for Understanding and
766 Treating Skeletal Diseases. *Traffic* **13**, 1307–1314 (2012).
767 71. Wagner, T., Dieckmann, M., Jaeger, S., Weggen, S. & Pietrzik, C. U. Stx5 is a novel interactor of VLDL-R to
768 affect its intracellular trafficking and processing. *Experimental Cell Research* **319**, 1956–1972 (2013).
769 72. Morelle, W. & Michalski, J.-C. Analysis of protein glycosylation by mass spectrometry. *Nature Protocols* **2**,
770 1585–1602 (2007).
771 73. Scherpenzeel, M. van, Steenbergen, G., Morava, E., Wevers, R. A. & Lefeber, D. J. High-resolution mass
772 spectrometry glycoprofiling of intact transferrin for diagnosis and subtype identification in the congenital
773 disorders of glycosylation. *Translational Research* **166**, 639-649.e1 (2015).
774 74. Vissers, L. E. L. M. *et al.* A de novo paradigm for mental retardation. *Nature Genetics* **42**, 1109–1112
775 (2010).
776 75. Nikopoulos, K. *et al.* Next-Generation Sequencing of a 40 Mb Linkage Interval Reveals TSPAN12 Mutations
777 in Patients with Familial Exudative Vitreoretinopathy. *The American Journal of Human Genetics* **86**, 240–
778 247 (2010).
779 76. Ran, F. A. *et al.* Genome engineering using the CRISPR-Cas9 system. *Nature Protocols* **8**, 2281–2308
780 (2013).
781 77. Schägger, H. Tricine–SDS-PAGE. *Nat Protoc* **1**, 16–22 (2006).
782 78. Wickham, H. *ggplot2: Elegant Graphics for Data Analysis*. (Springer-Verlag New York, 2016).
783
784